De-Orbiting Upper Stage Rocket Bodies Using a Deployable High Altitude Drag Sail

A Senior Project

presented to

the Faculty of the Aerospace Engineering Department

California Polytechnic State University, San Luis Obispo

In Partial Fulfillment

of the Requirements for the Degree

Bachelor of Science

by

Robert A. Hawkins and Joseph A. Palomares

June, 2012

De-Orbiting Upper Stage Rocket Bodies Using a Deployable High Altitude Drag Sail

Robert Hawkins[1] and Joseph Palomares1
California Polytechnic State University, San Luis Obispo, CA, 93407

This report examines the effectiveness of a drag sail to de-orbit upper stage rocket bodies. Many other perturbations contribute to the de-orbiting of these rocket bodies, and these perturbations will also be discussed briefly. This paper will show the length of time needed to force the altitudes of various launch vehicle stages with varying drag area sizes to less than 100 km. The upper stage of the Delta IV launch vehicle in an orbit with an altitude of 500 km will naturally de-orbit in 720 days but when equipped with a 20 m^2 drag sail, it will de-orbit in just 510 days. For this particular example the 29% reduction in de-orbit time is very significant. Multiple examples will be displayed in this report to demonstrate the effectiveness of such a drag sail.

Nomenclature

A	=	area (m^2)
a	=	acceleration (km/sec^2)
c	=	speed of light (3 x 10^8 m/s)
c_R	=	reflectivity coefficient
$\bar{c}(\tau_{min})$	=	temporary variable
C_B	=	ballistic coefficient (kg/m^2)
C_d	=	drag coefficient
F	=	force (N)
G	=	gravitational constant (6.67 x 10^{-11} $m^3/kg \cdot s^2$)
h	=	altitude (km)
H	=	scale height (km)
I	=	mass moment of inertia ($kg \cdot m^2$)
JD	=	Julian Date
J	=	Zonal harmonic
L	=	length (m)
m	=	mass (kg)
T	=	transformation matrix
Tdy	=	torque ($N \cdot m$)
μ	=	standard gravitational parameter (km^3/sec^2)
ω	=	argument of perigee
ω_o	=	orbital frequency (rad/s)
p_{SR}	=	solar radiation pressure (N/m^2)
φ_{inc}	=	solar incidence angle (rad)
r	=	radius (km)
Ω	=	right ascension of the ascending node
ρ	=	density (kg/m^3)
σ	=	mass moment of inertia simplification factor
τ_{min}	=	temporary variable
Θ	=	true anomaly (rad)
θ	=	pitch angle (rad)
v	=	velocity (km/s)

[1] Aerospace Engineering Undergraduate, Aerospace Engineering Department, 1 Grand Ave.

Subscripts

2	=	Second
3	=	Third
4	=	Fourth
5	=	Fifth
6	=	Sixth
ECI	=	earth centered inertial coordinate frame
ECEF	=	earth centered earth fixed coordinate frame
PQW	=	perifocal coordinate frame
NTW	=	satellite coordinate system
x	=	x-coordinate
y	=	y-coordinate
z	=	z-coordinate
$\odot$	=	sun
$\leftmoon$	=	moon
$\oplus$	=	earth

I. Introduction

ORBITAL debris has recently, and quickly, become one of the most serious concerns facing spacecraft today. Ever since Sputnik launched in 1957, the space environment has gone from an environment free of unused manmade hardware, to a junkyard, filled with millions of pieces of orbital debris. Although a great percentage of these pieces of debris are very small and don't appear as if they would be able to cause significant damage to operational spacecraft, the velocities at which these pieces are orbiting can be in excess of 7 km/s (about 15,000 miles per hour) and the relative velocities at impact can be anywhere from 9 to 14 km/s.[1] To put this in perspective, a small 1 kg piece of space debris that impacts with a velocity of 10 km/s has the same kinetic energy as an empty 18 wheeler going 180 miles per hour.

As the world rapidly evolves into a society that requires satellites for everything from watching television to credit card transactions, the orbital debris problem increases at an alarmingly high rate. From 1990 to 2010, the number of objects officially tracked by the United States Space Surveillance Network increased from about 7,500 objects to over 16,000.[2] This shockingly high number does not even include pieces of space debris that are less than 1 cm in diameter. The number of objects currently in orbit that fall into that category exceeds 100 million.[3]

One of the main reasons that space debris is a major issue for current and future space missions is the inevitability of collisions. The spike in orbital debris objects mentioned earlier was primarily due to two major events in which larger pieces of space debris were struck, either intentionally or accidently, and exploded into many smaller pieces of debris. The first major event was the intentional explosion of a Chinese weather satellite in 2007. This abnormal event couldn't have been anticipated by those trying to mitigate the orbital debris issue. Another collision between American and Russian communications satellites in 2009, however, is a perfect example of why the orbital debris issue is at the forefront of current aerospace innovation because it was simply an accident. All of the remaining larger pieces of orbital debris, like defunct satellites and rocket bodies, present more collision risks that could further contaminate usable space. In order to prevent future satellites and rocket bodies from becoming collision risks, prominent space exploration entities like NASA are beginning to mandate preventative measures to mitigate further accumulation.

NASA's mitigation procedure requires that any mission completely or partially operated by NASA must have completed an orbital debris assessment report and an end-of-mission plan. These two requirements examine the number of pieces of orbital debris that might be caused by the mission, their possibility for collisions, their expected orbits, as well as how long they will be in orbit.[4] The end-of-mission plan must detail what the mission architects plan to do to ensure that their hardware does not become useless debris once their mission is complete.[5] Geostationary Earth Orbiting (GEO) spacecraft have the option to maneuver to a graveyard orbit, approximately 300 km above GEO, while Low Earth Orbiting (LEO) spacecraft must reenter the atmosphere within 25 years.

According to a study by Anselmo, Rossi, Pardini, Cordelli, and Jehn on the future of orbital debris, using a variety of mitigation techniques going forward will greatly limit the amount of new space debris that will exist in

the year 2100. The study predicts that by mitigating debris generated by explosions, debris generated during mission lifetime operations, and by immediately de-orbiting all spacecraft below 2000 km at the end of their mission, the amount of orbital debris larger than 1 cm in LEO can be kept at around 13,000 items, instead of the predicted 35,000 items.[6]

Many LEO satellites opt to use various methods to de-orbit themselves including active thrust maneuvers, electrodynamic tethers, solar sails, and drag enhancing mechanisms such as balloons and drag sails. Primarily, drag enhancing mechanisms have been designed for the smaller scale pieces of debris such as small research satellites called CubeSats.[7] CubeSats are small 10 x 10 x 10 cm cube satellites that are generally used for educational or research based purposes.[8] Several designs for drag enhancement devices have been suggested over the past few years including a deployable pyramid structure, a 5 m^3 inflatable balloon, and an inflatable pillow-shaped de-orbit device.[9] All of these designs have produced analysis that suggest that de-orbit mechanisms can de-orbit the CubeSats at various altitudes within 25 years. Because the drag improvement mechanism functions effectively with the CubeSats, it makes sense that they would be logical choices in de-orbiting other types of spacecraft such as rocket bodies.

The objective of this report is to provide computational analysis that suggests that rocket bodies can be effectively de-orbited using a drag enhancing mechanism. This report will examine the effect the drag sail will have on the rocket body's stability throughout the duration of the sail's life, as well as all of the perturbations that are involved throughout the orbital lifetime.

II. Design

For the removal of debris at end-of-mission to be feasible, spacecraft must have the ability to de-orbit themselves. Assuming a spacecraft even has capability for such a maneuver, performing a de-orbiting burn is not preferable because it would shorten the life of spacecraft. Therefore implementation of a drag-inducing de-orbit device will be investigated here. The device will utilize a low-mass deployable 2-D sail that will increase the amount of surface area that is normal to the velocity vector. This drag will slow the spacecraft down, and slowly decrease the spacecraft's orbital altitude until it eventually reenters.

III. Analysis

Analysis was performed on the attitude as well as the orbit of the body. The orbital perturbations considered were non-spherical Earth in terms of J_2 through J_6 zonal harmonic perturbations, solar radiation pressure, drag, and the n-body effects of the Sun and Moon. Although the drag device only influences the acceleration due to drag and solar radiation pressure, other perturbations were included to accurately predict the orbit. Analysis was also conducted in the area of attitude determination of the body. The importance of this is that any rotational offset of the body will result in decreased area acting in the velocity vector.

The orbit will be propagated using MATLAB's built in ordinary differential solver ode113. This solver will differentiate the forces experienced by the body and, from initial position and velocity vector, propagate the position and velocity forward in time. From Newton's Law of Gravitation we have:

$$F = G\frac{m_1 m_2}{r^2} \tag{1}$$

where G is the gravitational constant, m_1 and m_2 are the masses of the two objects and r is the distance between the two objects.[10] For a body orbiting Earth a common substitution for the above equation is to replace the gravitational constant and m_1 with Earth's standard gravitational parameter, μ. Further simplification can be made by dividing both sides of the equation by the mass of m_2, the mass of the body, yielding Eq. 2.[11]

$$a = -\frac{\mu}{r^2} \tag{2}$$

To propagate the orbit from a more than one dimensional standpoint the acceleration term as well as the position term must be made into vectors. Addition of other accelerations, such as the perturbation accounted for in this analysis, must also be added in before the equation is run through the ordinary differential solver, as seen in Eq. 3.[11]

$$\vec{a} = -\frac{\mu}{r^3}\vec{r} + \sum \vec{a}_{\text{perturbations}} \tag{3}$$

It is also important to note that all operations run though the ordinary differential solver will be in the common ECI coordinate frame.

A. Acceleration Perturbations Due to Earth's Zonal Harmonics

In a standard two-body problem it is assumed that both bodies are point masses, this is of course untrue for any physical body. Since the Earth is spinning it bulges at its center, an effect known as oblateness. Centrifugal force causes the Earth to be wider at the equator than at the poles. Ocean tides, mountain ranges, and simply the different densities of material that make up the Earth all contribute to the erroneous results when Earth is treated as a point mass. For the accuracy needed for this analysis zonal harmonics will be used to estimate the perturbation due to Earth's oblateness. This method defines harmonic regions based only on latitude, giving no concern to different harmonic values based on longitude. The harmonics are named by the scheme $J_{l,m}$, in spherical harmonics $m = 0$ and is therefore usually neglected and l is equal to the number of harmonic zone minus one. For example, $J_{2,0}$ is often referred to simply as J_2 and contains three different zones. To calculate the perturbations from the second spherical harmonic the following Legendre polynomial will be used,

$$R_2 = -\frac{3J_2\mu_\oplus {R_\oplus}^2}{2r^3}\left(\frac{r_K}{r}\right)^2 + \frac{J_2\mu_\oplus {R_\oplus}^2}{2r^3} \tag{4}$$

where J_2 is the Legendre coefficient, $\mu_\oplus$ is the standard gravitational parameter of Earth, $R_\oplus$ is the radius of Earth, and r is the radius from Earth to the spacecraft.[11] To calculate the actual acceleration due to the second spherical harmonic the partial derivative of Eq. 4 must be taken with respect to each coordinate direction, resulting in Eqs. 4, 5, and 6.[12]

$$a_{J_{2_I}} = \frac{\partial R_2}{\partial I} = -\frac{3J_2\mu_\oplus {R_\oplus}^2 r_I}{2r^5}\left(1 - \frac{5{r_K}^2}{r^2}\right) \tag{5}$$

$$a_{J_{2_J}} = \frac{\partial R_2}{\partial J} = -\frac{3J_2\mu_\oplus {R_\oplus}^2 r_J}{2r^5}\left(1 - \frac{5{r_K}^2}{r^2}\right) \tag{6}$$

$$a_{J_{2_K}} = \frac{\partial R_2}{\partial K} = -\frac{3J_2\mu_\oplus {R_\oplus}^2 r_K}{2r^5}\left(3 - \frac{5{r_K}^2}{r^2}\right) \tag{7}$$

It is important to note that Eq. 5 and Eq. 6 are very similar, while equation Eq. 7 is quite different. This is due to the r_K term originally in equation Eq. 4 and taking the partial derivative with respect to it yields a much different result. The method of taking the partial derivatives is the same for all the zonal harmonic terms here, thusly only the Legendre polynomials seen in Eqs. 8, 9, 10, and 11 are shown here.[13]

$$R_3 = -\frac{J_3\mu_\oplus}{2r}\left(\frac{R_\oplus}{r}\right)^3\left[5\left(\frac{r_K}{r}\right)^3 - 3\frac{r_K}{r}\right] \tag{8}$$

$$R_4 = -\frac{J_4\mu_\oplus}{8r}\left(\frac{R_\oplus}{r}\right)^4\left[35\left(\frac{r_K}{r}\right)^4 - 30\left(\frac{r_K}{r}\right)^2 + 3\right] \tag{9}$$

$$R_5 = -\frac{J_5\mu_\oplus r_K}{8r^2}\left(\frac{R_\oplus}{r}\right)^5\left[15 - 70\left(\frac{r_K}{r}\right)^2 + 63\left(\frac{r_K}{r}\right)^4\right] \tag{10}$$

$$R_6 = \frac{J_6\mu_\oplus r_K}{16r}\left(\frac{R_\oplus}{r}\right)^6\left[5 - 105\left(\frac{r_K}{r}\right)^2 + 315\left(\frac{r_K}{r}\right)^4 - 231\left(\frac{r_K}{r}\right)^6\right] \tag{11}$$

Finally, all of the harmonic terms are added to each other, as seen in Eq. 12.[11]

$$a = \begin{bmatrix} a_{J_{2_I}} + a_{J_{3_I}} + a_{J_{4_I}} + a_{J_{5_I}} + a_{J_{6_I}} \\ a_{J_{2_J}} + a_{J_{3_J}} + a_{J_{4_J}} + a_{J_{5_J}} + a_{J_{6_J}} \\ a_{J_{2_K}} + a_{J_{3_K}} + a_{J_{4_K}} + a_{J_{5_K}} + a_{J_{6_K}} \end{bmatrix} \tag{12}$$

All of the zonal coefficients can be found in Appendix A. It should be noted that all of the spacecraft position terms, r, and the resulting acceleration terms are in the ECEF frame. This means a coordinate transformation from the ECI frame to the ECEF frame must be preformed, then back again. These coordinate transformations require an input of not only the vectors that are being transformed, but also the Julian date. Since the ECEF frame is fixed with respect to Earth such that I_{ECEF} always points out of longitude 0°, latitude 0° and the ECI frame rotates about the Earth's poles such that the I_{ECI} always points towards the First Point of Aries, γ. If the assumption is made that Earth only rotates about its poles, then the only angle needed is the Greenwich sidereal time, θ, since K_{ECEF} is assumed to be equal to K_{ECI}. The algorithm used to calculate the Greenwich sidereal time can be found in Appendix B. A diagram of the conversion between the ECEF and ECI coordinate frames can be seen in Figure 1.

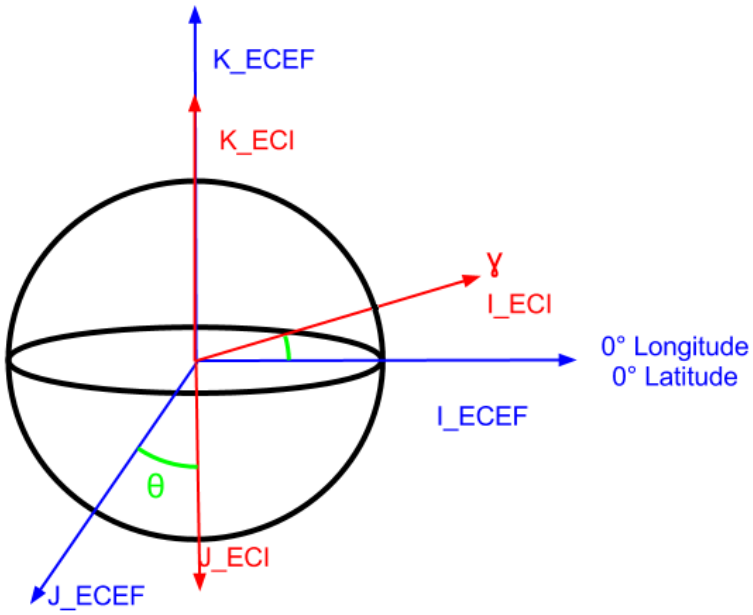

Figure 1. Earth with ECEF and ECI coordinate frames.

The coordinate transformation for the position vector only requires the use of a single transformation matrix using the Greenwich sidereal time. The equation for the coordinate transformation between a position vector in ECI to a position vector in ECEF is shown:

$$r_{ECEF} = [T]\, r_{ECI} \tag{13}$$

where T is the transformation matrix,

$$[T] = \begin{bmatrix} \cos\theta & \sin\theta & 0 \\ -\sin\theta & \cos\theta & 0 \\ 0 & 0 & 1 \end{bmatrix} \tag{14}$$

and where θ is the Greenwich sidereal time. The transformations for the velocity and acceleration vectors are not so simple.[14] Since the coordinate frames are rotating with respect to one another, additional terms must be added. For the proper velocity vector transformation the derivative of the position transformation equation must be preformed, as shown in Eqs. 15, 16, and 17.

$$v_{ECEF} = \frac{d}{dt}\, r_{ECEF} \tag{15}$$

$$v_{ECEF} = \frac{d}{dt}\, ([T]\, r_{ECI}) \tag{16}$$

$$v_{ECEF} = [T]\, v_{ECI} + [\dot{T}]\, r_{ECI} \tag{17}$$

Where $\dot{T}$ is the derivative of the T transformation matrix,

$$[\dot{T}] = \begin{bmatrix} -\omega_{\oplus}\sin\theta & \omega_{\oplus}\cos\theta & 0 \\ -\omega_{\oplus}\cos\theta & -\omega_{\oplus}\sin\theta & 0 \\ 0 & 0 & 0 \end{bmatrix} \tag{18}$$

and where $\omega_{\oplus}$ is the spin rate of the Earth. Likewise for the transformation of the acceleration term we get,

$$a_{ECEF} = \frac{d}{dt}\, v_{ECEF} \tag{19}$$

$$a_{ECEF} = \frac{d}{dt}\, ([T]\, v_{ECI} + [\dot{T}]\, r_{ECI}) \tag{20}$$

$$a_{ECEF} = [\ddot{T}]\, r_{ECI} + 2[\dot{T}]\, v_{ECI} + [T]\, a_{ECI} \tag{21}$$

where $\ddot{T}$ is the double derivative of the T transformation matrix seen in Eq. 22.

$$[\ddot{T}] = \begin{bmatrix} -\omega_{\oplus}{}^2 \cos\theta & -\omega_{\oplus}{}^2 \sin\theta & 0 \\ \omega_{\oplus}{}^2 \sin\theta & -\omega_{\oplus}{}^2 \cos\theta & 0 \\ 0 & 0 & 0 \end{bmatrix} \tag{22}$$

For the transformation from the ECEF back to the ECI frame one must simply take the transpose of each of the transformation matrices. Although all transformations are shown below, the only transformation of interest is the transformation of the acceleration term.

$$r_{ECI} = [T]^T r_{ECEF} \tag{23}$$

$$v_{ECI} = [T]^T v_{ECEF} + [\dot{T}]^T r_{ECEF} \tag{23}$$

$$a_{ECI} = [\ddot{T}]^T r_{ECEF} + 2[\dot{T}]^T v_{ECEF} + [T]^T a_{ECEF} \tag{24}$$

Although the zonal harmonics equations only call for the transformation of the position vector we must transform an arbitrary acceleration vector from the ECI to ECEF frames to add to the resulting acceleration from the harmonics equations. After this the acceleration term is to be transformed back to the ECI frame. A simplified diagram of this algorithm can be found in Appendix C.

B. Acceleration Perturbations Due to N-Body Effects

An n-body analysis was done to calculate the perturbing forces due to the gravitational force exerted on the spacecraft from both the Sun and the Moon. Simply using Eq. 2 for calculating the gravitational effect of the Sun and Moon will yield erroneous results as there is a coordinate ambiguity. To keep all terms in the ECI frame the following equation is promising.[12]

$$\vec{a}_n = \mu_n \left(\frac{\vec{r}_{sat\_n}}{{r_{sat\_n}}^3} - \frac{\vec{r}_{\oplus\_n}}{{r_{\oplus\_n}}^3} \right) \tag{25}$$

Where μ is a standard gravitational parameter and the subscripts *n* and *sat* represent the n-body in question and the spacecraft respectively. The convention for a variable with two subscripts is that it is from the first subscript to the second. For example, X_{A_B} means from the A to the B. In the equation above the term $\vec{r}_{sat\_n}$ is the position vector of the spacecraft from the n-body. Figure 2 shows a graphical representation of Eq. 25.

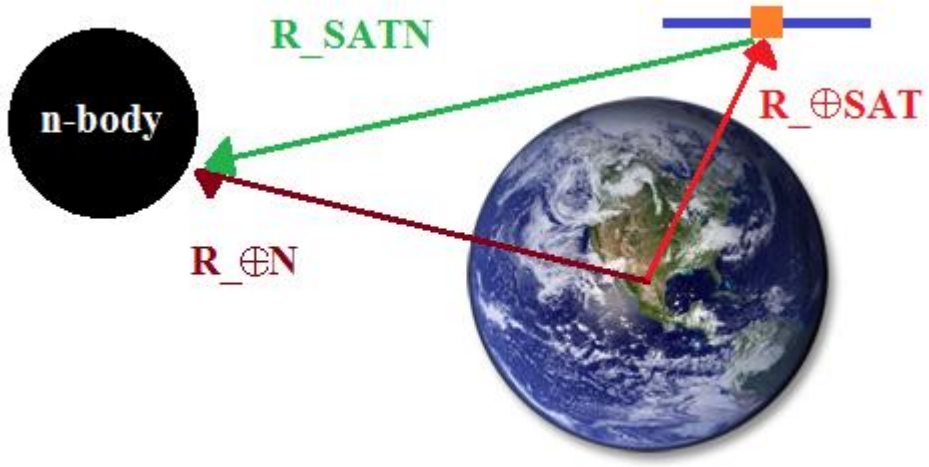

Figure 2. Vector description of n-body interaction.

Errors using Eq. 25 result from numerical compounded differences from the small numbers seen from the term in the parenthesis. The following equation has been chosen instead, it results from a Taylor series expansion done by Geyling and Westerman.[12]

$$\vec{a}_n \cong -\frac{\mu_n}{{r_{\oplus}}^3} \left[\vec{r}_{\oplus\_sat} - 3\vec{r}_{\oplus\_n} \frac{\vec{r}_{\oplus\_sat} \cdot \vec{r}_{\oplus\_n}}{{r_{\oplus\_n}}^3} - \frac{15}{2} \left(\frac{\vec{r}_{\oplus\_sat} \cdot \vec{r}_{\oplus\_n}}{{r_{\oplus\_n}}^3} \right)^2 \vec{r}_{\oplus\_n} \right] \tag{26}$$

All of the position vectors, as well as the resulting acceleration vector, are all in the ECI frame. Vallado shows a simplified way of calculating the position vectors from both the Sun and the Moon. The algorithms for

how to calculate the position vector from the Earth to the Sun and Moon in the ECI frame can be found in Appendix D and Appendix E respectively.

C. Acceleration Perturbations Due to Solar Radiation Pressure

Since light carries energy with it, it exerts a force on an object when the object is struck by a photon. Using Einstein's theory of special theory of relativity, the relationship between the solar flux and the speed of light is defined by using the following equation,

$$P_{SR} = \frac{SF}{c} \tag{27}$$

where *SF* is the solar flux, *c* is the speed of light, and P_{SR} is the solar radiation pressure.[12] A commonly accepted average solar flux for objects at 1 AU from the Sun is 1367 Wm^{-2}. Knowing this the calculation for finding solar radiation pressure can be completed.

$$P_{SR} = \frac{1367\frac{W}{m^2}}{3\times10^8\frac{m}{s}} = 4.57e-6\ \frac{N}{m^2} \tag{28}$$

From this the following equation can be utilized to calculate the solar radiation pressure inflicted on a body around Earth.

$$\vec{a}_{SRP} = P_{SR}c_R A_{\odot}\hat{r}_{\odot\_SAT} \tag{29}$$

Where a_{SRP} is the acceleration vector, c_R is the reflectivity coefficient, $A_{\odot}$ is the area of the body that is exposed to the Sun, and $\hat{r}_{\odot\_SAT}$ is the unit vector of the position of the spacecraft in relation to the Sun in the ECI frame. The position vector from the Sun to the spacecraft is important because that is the direction that the solar radiation pressure will act in. This vector has already been calculated for determining the n-body interaction of the Sun, and the algorithm for calculating this vector can be found in Appendix D.

Further consideration must be given to the reflectivity coefficient and the area exposed to the Sun. For the solar radiation to take effect the body must have an amount of area facing the Sun; this makes knowing orientation of the body very important and attitude determination must be calculated. An accurate reflectivity coefficient is also needed to calculate the effect of solar radiation pressure. When light comes into contact with a material it either reflects the light, absorbs the light, or transmits the light, as displayed in Figure 3.

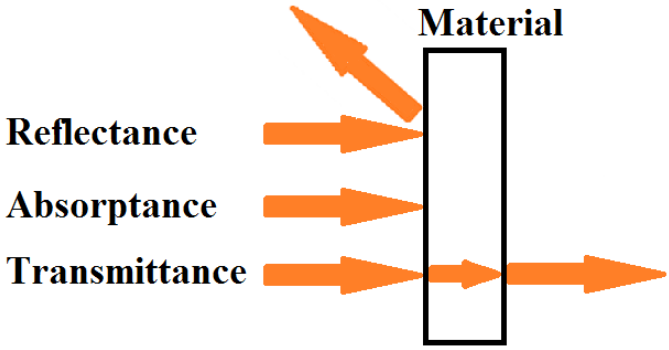

Figure 3. Reflectance, absorptance, and transmittance of a material.

When the light is reflected the reflectivity coefficient is equal to 2, when the light is absorbed by the material the reflectivity coefficient is 1, finally when the light simply passes through the material the reflectivity coefficient is 0. Knowing the reflectivity coefficient of a body is often a quite difficult task which requires the knowledge of how much light is reflected and absorbed by the spacecrafts different surfaces. Furthermore since many different materials may cover the spacecraft, the orientation of the spacecraft becomes important again as the entire spacecrafts reflectivity coefficient is needed for any orientation. The knowledge of a material's reflectivity coefficient is complicated further when a surface's properties degradation is taken into account due to the space environment. For this simulation a highly reflective surface will be used with a c_R of 1.9, and no degradation is assumed. It is further assumed that the area of the sail is much greater the area of the spacecraft so that only the area of the sail and the reflectivity coefficient of the sail is taken into account.

1) Eclipse Check

Calculations were also preformed to neglect solar radiation pressure when the spacecraft is in umbra; calculations were not done to account for the penumbra. Analysis was performed to find whether or not a line of sight existed between the Sun and the spacecraft, although this is not a true umbra it will be assumed to be acceptable. A diagram of line of sight can be seen in Figure 4.

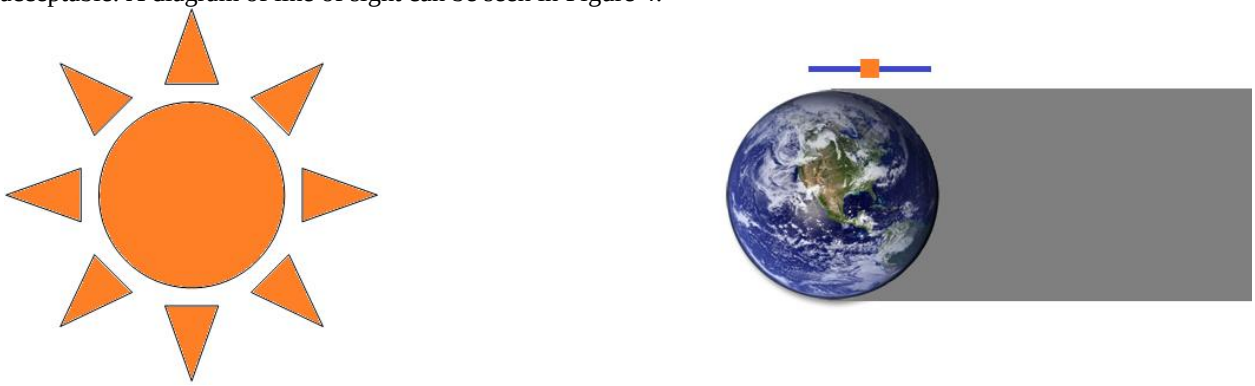

Figure 4. Absence of a line of sight between a spacecraft and the Sun shown as darkness.

The line of sight algorithm is taken from Vallado, and can be found in the Eq. 29.[12]

$$\tau_{min} = \frac{|\vec{r}_{sat}|^2 - (\vec{r}_{sat} \cdot \vec{r}_{\odot})}{|\vec{r}_{sat}|^2 + |\vec{r}_{\odot}|^2 - 2(\vec{r}_{sat} \cdot \vec{r}_{\odot})} \tag{29}$$

If τ_{min} is less than 0 or greater than 1, then there is a line of sight between the spacecraft and the Sun, and solar radiation pressure is acting on the body. If τ_{min} is less than 1 and greater than 0, the following equation must be calculated for;

$$|\vec{c}(\tau_{min})|^2 = \frac{(1-\tau_{min})|\vec{r}_{sat}|^2 + (\vec{r}_{sat} \cdot \vec{r}_{\odot})\tau_{min}}{R_{\oplus}{}^2} \tag{30}$$

if $|\vec{c}(\tau_{min})|^2$ is less than 1 than no line of sight exists, if not then there is a line of sight.

2) Solar Incidence Angle

The perturbations caused by solar radiation pressure are not only dependent on the amount of time spent in the sun, but also upon the orientation and angle at which the solar radiation pressure hits the spacecraft. Over the course of the orbital period, the spacecraft will be exposed to the sun at many different angles. This angle will be referred to as the incident angle, and will be denoted by the variable φ_{inc}. This incident angle is the angular displacement between the vector from the spacecraft to the sun, and the surface normal vector. In order to calculate this angle, the only two vectors needed are the surface normal vector, and the sun vector, both in the Earth Centered Inertial frame so that it may be utilized in the rest of the analysis. The first thing that needs to be done is to find the surface normal vector for the spacecraft in the spacecrafts NTW frame. This can be found by taking the unit normal vector and multiplying it through a rotation matrix about the pitch axis, and multiplying that rotation matrix by the spacecraft unit normal vector as shown below

$$\hat{n}_{NTW} = \begin{bmatrix} 1 \\ 0 \\ 0 \end{bmatrix} \begin{bmatrix} \cos(\theta) & 0 & -\sin(\theta) \\ 0 & 1 & 0 \\ \sin(\theta) & 0 & \cos(\theta) \end{bmatrix} \tag{31}$$

where θ is the angle about the pitch axis.[11] That angle will be discussed more in the atmospheric drag section of this report. Once the unit normal vector is in the spacecraft's NTW frame, a second transformation must be done to put the matrix into the ECI frame. This coordinate transformation is a bit more complicated and uses the transformation series shown below

$$\hat{n}_{ECI} = \left\{ \begin{bmatrix} \cos(\omega) & \sin(\omega) & 0 \\ -\sin(\omega) & \cos(\omega) & 0 \\ 0 & 0 & 1 \end{bmatrix} \begin{bmatrix} 1 & 0 & 0 \\ 0 & \cos(i) & \sin(i) \\ 0 & -\sin(i) & \cos(i) \end{bmatrix} \begin{bmatrix} \cos(\Omega) & \sin(\Omega) & 0 \\ -\sin(\Omega) & \cos(\Omega) & 0 \\ 0 & 0 & 1 \end{bmatrix} \right\}' \begin{bmatrix} \cos(-\Theta) & \sin(-\Theta) & 0 \\ -\sin(-\Theta) & \cos(-\Theta) & 0 \\ 0 & 0 & 1 \end{bmatrix} \hat{n}_{NTW} \tag{32}$$

where ω is the argument of perigee of the orbit, i is the inclination in radians of the orbit, Ω is the right ascension of the ascending node, and Θ is the true anomaly in radians. Once the surface normal is in the ECI frame, it is

necessary to find the sun vector in ECI frame in order to find the angle between the two vectors. While finding the solar radiation pressure, the position vector of the sun relative to the Earth in ECI frame was found using the Julian Date, so this vector has already been found during previous analysis. At this point, a simple dot product and simple algebra will yield the incidence angle. The dot product is shown below

$$DP = \bar{R}_{SUN_{ECI}} \cdot \hat{n}_{ECI} \tag{33}$$

This dot product will yield a single numerical value which is used to find the incident angle as shown in the following equation

$$\varphi_{inc} = \frac{DP}{R_{SUN_{ECI}} \| \hat{n}_{ECI} \|} \tag{34}$$

This incident angle will be used in conjunction with the solar radiation pressure and the eclipse checking equations to achieve a more accurate simulation of the affects of solar radiation pressure on the drag sail.

D. Acceleration Perturbations Due to Atmospheric Drag

All of the perturbations previously discussed in this report were perturbations that are extremely difficult to manipulate in any useful way. N-body and zonal harmonic perturbations for example are natural perturbations and impossible to manipulate. Atmospheric drag is one perturbation that actually can be altered and used to the advantage of engineers. Because the acceleration due to the force of drag is dependent upon the cross sectional area, an increase in cross sectional area directly increases the acceleration. In this way, large cross sectional areas can be used to create large accelerations which will eventually lower the energy of the rocket bodies enough to de-orbit them. The atmospheric drag mostly affects the eccentricity and the semimajor axis of the orbit, but also has minor effects on the other orbital elements throughout the lifetime of the space vehicle. For elliptical orbits, the radius of perigee of the orbit tends to stay fairly constant, while the radius of apogee shrinks along with the eccentricity, slowly circularizing the orbit.[10] This effect can be seen in Figure 5.

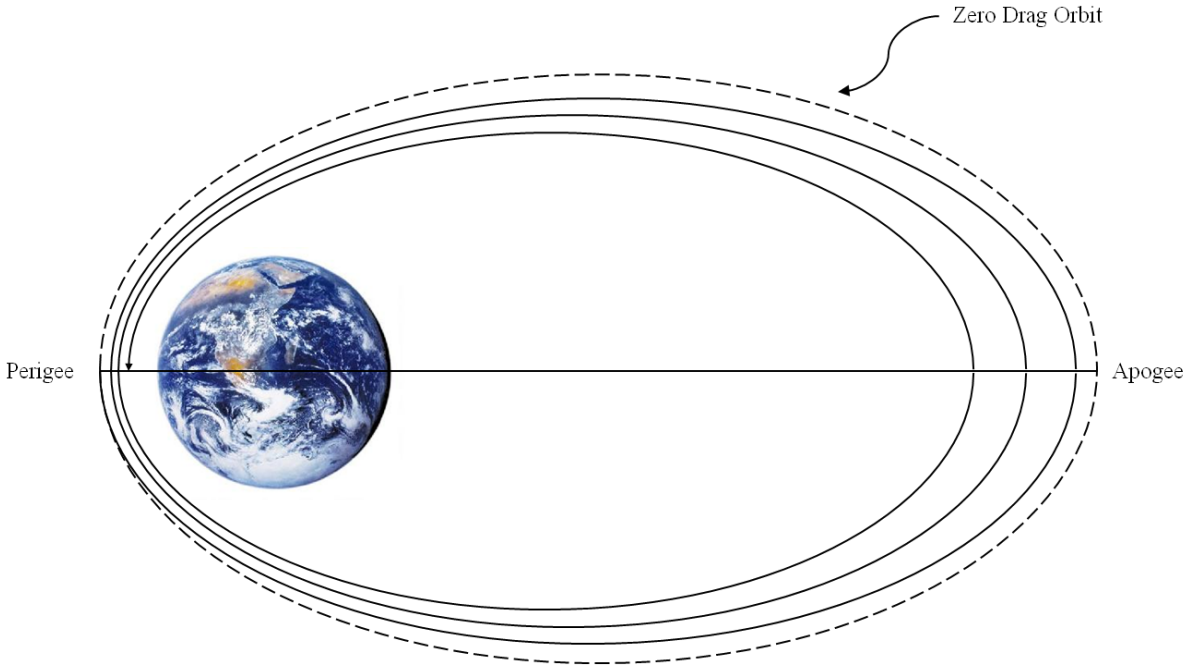

Figure 5. Effect of Atmospheric Drag on Orbit Eccentricity

While the effects of drag are exaggerated in Figure 5, the effect over a long period of time is clearly shown. The dotted line depicts the orbit as it would continue if there were no perturbations on it at all. The sequence of solid lines shows an exaggerated depiction of the effect drag will have on this particular orbit. The eccentricity of this orbit approaches zero as the radius of apogee gets smaller. As the radius of perigee gets smaller, the orbit will eventually get close enough to Earth to de-orbit.

Spacecraft in orbit experience their highest velocities at their radius of perigee. As the radius of perigee decreases, the velocity of the object at its radius of perigee increases. The interesting thing about this is that as

the radius of perigee decreases, the spacecraft is getting closer and closer to earth, and therefore increasing in drag force. The lower the altitude of the spacecraft, the higher the density of particles that the body will encounter, and the higher the drag force will be. This fact causes a brand of thinking which is often referred to as the drag paradox.[10] This paradox is caused by the energy transfer that is taking place as the force of drag is imparted on the satellite. It can be shown that any force which adds total energy to the body will make the orbit larger and decrease the kinetic energy, and that any force which takes away total energy will make the orbit smaller and increase kinetic energy.

Although at higher altitudes, n-body and solar radiation pressure are the dominant perturbations, the acceleration due to atmospheric drag is the second largest perturbation on lower altitude orbits, after Earth's oblateness. Many conclusions can be drawn by examining the equation for the acceleration due to atmospheric drag, which is given below in Eq. 35

$$a_{drag} = -\frac{1}{2} C_d A \frac{\rho}{m} v^2 \tag{35}$$

where C_d is the drag coefficient, A is the cross sectional area in the drag vector, ρ is the density, m is the mass of the rocket body, and v is the magnitude of the rocket body's velocity vector. [12] Although Eq. 35 looks relatively simple, one of the difficulties in atmospheric drag analysis is that some of the values are very difficult to find.

For instance, the drag coefficient C_d is a dimensionless number that describes how severely the body will be affected by the force of drag. This number is difficult to calculate and is different for every piece of space hardware. Frequently the drag coefficient is simply assumed to be 2.2 for plate-plate models of satellites, and about 2.0 or 2.1 for satellites that are modeled as spheres.[10] Shown in the table below is a table with the kind of drag coefficients that past spacecraft have been given based on their approximate shape and size.[11]

Table 1. Drag Coefficients of Previously Flown Spacecraft

Satellite	Mass (kg)	Shape	Min C_d	Max C_d	Min Ballistic Coefficient (kg/m^2)	Max Ballistic Coefficient (kg/m^2)
Oscar-1	5	Box	2	4	16.7	42.8
Vanguard-2	9	Sphere	2	2	23.5	23.5
Viking	277	Octagon	2.6	4	30.8	128
OSO-7	634	9-Sided	2.9	3.67	165	437
HEAO-2	3,150	Hexagon	2.83	4	80.1	174
LDEF-1	9,695	12-Face	2.67	4	93.1	169
SkyLab	76,136	Cylinder	3.5	4	47.1	410

The drag coefficients shown in Table 1 are based on the cross sectional area normal to the drag vector, as well as the shape, size, and orientation of the satellites shown. Most of the satellites shown have a maximum drag coefficient of four, and all have a minimum drag coefficient greater than two. The only spacecraft on this table that includes solar panels is SkyLab, which has the largest minimum drag coefficient. For the analysis detailed in this report, the drag coefficient is assumed to be constant at 2.2.[11] The ballistic coefficient, which is also shown in Table 1, is a parameter that is often times held constant in orbital analysis, but varies greatly depending on orientation and will therefore not be considered constant in this analysis. The equation for the ballistic coefficient is given in the simple equation below as

$$C_B = \frac{m}{C_D A} \tag{36}$$

Where m is the mass of the body, C_D is the drag coefficient, and A is the cross sectional area normal to the drag vector.

Additionally, the cross sectional area normal to the drag vector is not always easy to find either. Although some spacecraft are stabilized in such a way that their cross sectional area is designed to be constant, small disturbances, including the torque due to drag, or nutation errors may cause the spacecraft to change its orientation such that the area is not constant. Even small errors in the cross sectional area need to be carefully monitored in order to achieve an accurate simulation of the effects of atmospheric drag. If a spacecraft were to be tumbling, the cross sectional area could be changing enormously and be impossible to estimate. If a spacecraft were to change its attitude in order to perform various mission specific operations, the attitude changes would have to be taken into account in order to estimate the cross sectional area. For instance, if a spacecraft was

equipped with movable solar panels such that the panels adjusted their positioning to always have their maximum area in the sun, the area in the drag vector would inevitably change. An example of this type of maneuver is shown in the figure below. The solar panels in the figure below have a total surface area of one square meter.

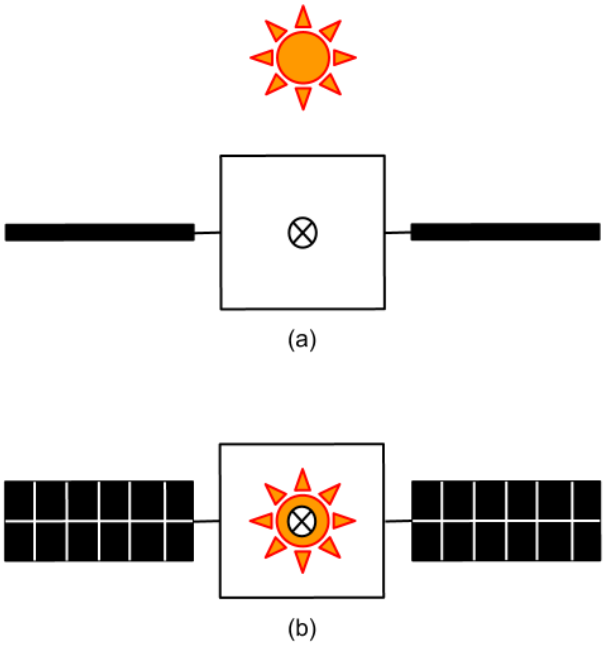

Figure 6. Cross Sectional Area Based on Spacecraft Orientation

In Figure 6a the solar panels are pointed at the sun and are perpendicular to the drag vector, which is marked at the center of the spacecraft. In Figure 6b however, the sun is in line with the drag vector, so the solar panels are fully exposed to the force of drag. In the orientation depicted in Figure 6b the cross sectional area has increased, and the drag force will be more severe on the spacecraft than it would be if the spacecraft were in the orientation shown in Figure 6a.

The other variable that varies a significant amount throughout the rocket body's lifetime is the density of particles that the body is exposed to. The density of these particles is not as commonly known as the density of the air on Earth, and is the most difficult part of analyzing the acceleration due to drag. In order to find the density of the particles in an orbital path many different methods for estimating the density have been created, each with a different combination of computational intensity and accuracy. The difficult thing about calculating the density is that it is dependent on so many other variables such as location around earth, time of day, a rotating atmosphere, ocean tides, solar rotation cycle, and much more.

1) Density Model

Because the density of particles in space is such an unknown variable, and is exceedingly difficult to know with any deal of certainty, there have been numerous attempts to model the density as a function of orbital altitude that include everything from magnetic storm variations right down to winds and weather patterns. The affect that all of these events have on the particle density is complex and has been gathered through years of experimental data to form mathematical models. One of the simplest models that have been used to model the atmosphere is the U.S. Standard Atmosphere 1976 model. This model represents the steady state atmosphere at a moderate solar activity. This model has a low altitude section and a high altitude section which are calculated separately. The lower altitude section is calculated using equations for temperature and pressure, while the upper atmospheric model focuses on numerical integration techniques to find the density. The density and mean free path for the lower altitude section and the beginning portion of the high altitude section is shown in Figure 7. The definition of mean free path is the distance traveled by a particle in between collisions, which for high density regions is very small; this distance grows as density decreases.

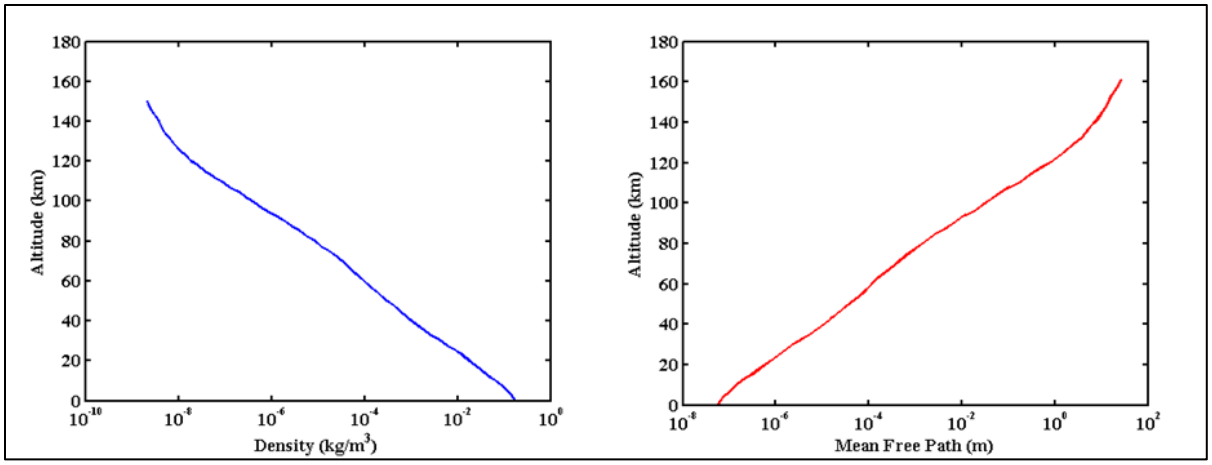

Figure 7. Density and Mean Free Path as a Function of Altitude Using U.S. Standard Atmosphere Model

Over the same altitude range, it seems intuitive that the correlations of density and mean free path to altitude would be opposites. As the density of the particles decreases, there are fewer particles for moving particles to collide with. This means that the distance between the particles, or the mean free path, is larger. While the standard atmosphere model is sufficient for lower altitudes and is very useful for analysis of aircraft, a model that is more accurate at higher altitudes needed to be used for this analysis and so other models were also considered.

One of the other models that was looked at provided atmospheric data based on previously flown mission. The MSIS-86 atmospheric model used data from rocket flights and satellites to piece together atmospheric data that included neutral temperature, exospheric temperatures, densities of numerous gasses at various altitudes, as well as total density. The atmospheric model continued to improve as the model began to examine space shuttle flights and sounding rockets until it became a new atmospheric model called the MSIS-90. This model takes into effect many sources of uncertainty in density calculations including solar variation. One of the main solar variations that it takes into account is what is known as the F10.7 index. This value is used to interpret the contribution that solar flux gives to atmospheric density. It is unfortunately impossible to measure the solar flux from the Earth's surface because the Earth's atmosphere filters out the ultra-violet radiation. It has been found that the F10.7 index can be used to estimate the solar flux because both F10.7 solar radiation and ultra violet radiation. It varies over time and cycles roughly every eleven years. The atmospheric density is shown with average solar activity as well as variable solar activity in the figure below.

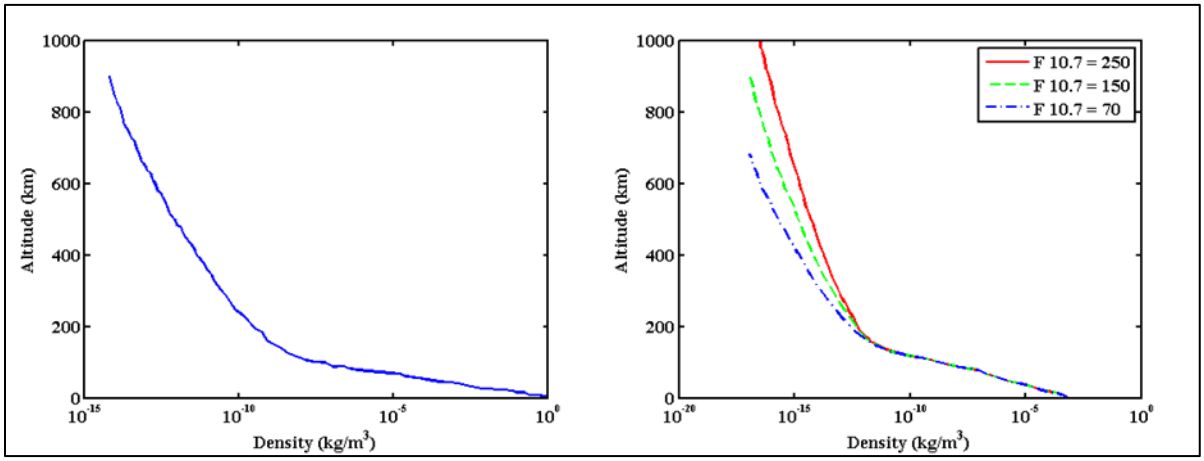

Figure 8. Density as a Function of Solar Acitivity Using MSIS-90 Atmospheric Model

The graph on the left in Figure 8 shows the atmospheric density at average solar activity, which in this case has been taken to be 150 solar flux units or SFU's. A solar flux unit is equal to 1 x 10^{-22} Watts*m^{-2}*s^{-1}. The graph on the right in Figure 8 shows the dotted green 150 SFU line sandwiched between a solar activity of 250 SFU's depicted as the solid red line, and a solar activity of 70 SFU shown as a dashed blue line. These graphs clearly demonstrate that the solar activity has an effect on the density at higher altitudes, but hardly alters it at all at

altitudes lower than 200 km. This model is very sophisticated and takes into account a great many factors in calculating atmospheric density, but due to its complexity and excessive computation requirements, a simpler density model was selected to do the analysis.

The exponential atmospheric model is a simple model that assumes the density of the atmosphere gets smaller exponentially as the altitude of the orbit increases. The other assumption that this model makes is that the density distribution is a uniform sphere where the density of particles varies according to one very simple equation shown below

$$\rho = \rho_0 e^{\left[-\frac{h_{ellp}-h_0}{H}\right]} \tag{37}$$

where ρ_0 is a reference density, h_{ellp} is the actual altitude of the spacecraft, h_0 is a reference altitude, and H is a scale height. The actual altitude of the spacecraft can be calculated by simply calculating the norm of the radius vector in the Earth Centered Inertial frame, but the reference and scale values are not intuitive. The values for these variables have been found in David Vallado's *Fundamentals of Astrodynamics and Applications* and are listed in the table below.

Table 2. Exponential Atmospheric Model Reference Variables[12]

Actual Altitude h_{ellp} (km)	Reference Altitude h_0 (km)	Reference Density ρ_0 (kg/m^3)	Scale Height H (km)	Actual Altitude h_{ellp} (km)	Reference Altitude h_0 (km)	Reference Density ρ_0 (kg/m^3)	Scale Height H (km)
0 – 25	0	1.225	7.249	150 – 180	150	2.070×10^{-9}	22.523
25 – 30	25	3.899×10^{-2}	6.349	180 – 200	180	5.464×10^{-10}	29.740
30 – 40	30	1.774×10^{-2}	6.682	200 – 250	200	2.789×10^{-10}	37.105
40 – 50	40	3.972×10^{-3}	7.554	250 – 300	250	7.248×10^{-11}	45.546
50 – 60	50	1.057×10^{-3}	8.382	300 – 350	300	2.418×10^{-11}	53.628
60 – 70	60	3.206×10^{-4}	7.714	350 – 400	350	9.518×10^{-12}	53.298
70 – 80	70	8.770×10^{-5}	6.549	400 – 450	400	3.725×10^{-12}	58.515
80 – 90	80	1.905×10^{-5}	5.799	450 – 500	450	1.585×10^{-12}	60.828
90 – 100	90	3.396×10^{-6}	5.382	500 – 600	500	6.967×10^{-13}	63.822
100 – 110	100	5.297×10^{-7}	5.877	600 – 700	600	1.454×10^{-13}	71.835
110 – 120	110	9.661×10^{-8}	7.263	700 – 800	700	3.614×10^{-14}	88.667
120 – 130	120	2.438×10^{-8}	9.473	800 – 900	800	1.170×10^{-14}	124.64
130 – 140	130	8.484×10^{-9}	12.636	900 – 1000	900	5.245×10^{-15}	181.05
140 – 150	140	3.845×10^{-9}	16.149	1000 +	1000	3.019×10^{-15}	268.00

While the exponential atmospheric model is not the most accurate model available for density, by using these intervals and reference values, it is possible to mitigate the inaccuracies enough to simulate the drag effects for design and general studies.[10] This model is the model that is used for the analysis detailed in this report. A sample calculation for the atmospheric density experienced by a spacecraft at 425 km is shown below. This sample calculation utilizes Eq. 37 and reference numbers from Table 2.

$$\rho = \rho_0 e^{\left[-\frac{h_{ellp}-h_0}{H}\right]} \tag{38}$$

$$\rho = 3.725 \times 10^{-12} e^{\left[-\frac{425-400}{58.515}\right]} \tag{39}$$

$$\rho = 2.43 \times 10^{-12}\,\frac{kg}{m^3} \tag{40}$$

This calculation shows that the density of the drag inducing particles is extremely low at that high of an altitude, but over an extended period of time, even a density that low can take its toll on a spacecrafts orbit.

2) Gravity Gradient Stabilization

The drag perturbations caused by this density, as well as all of the previously discussed perturbations, are the reasons that many past spacecrafts have become unstable over the course of their mission lifetime. It is because of these perturbations that attitude control methods have needed to be used. As spacecraft have evolved over the

years, so too have the methods for controlling a spacecrafts attitude. There are many ways to maintain stabilization both passive and active, including thrusters, spin stabilization, and of course gravity gradient stabilization. Without these methods of attitude control, many satellite missions would be unable to perform their necessary tasks.

In the case of this particular project, a passive method is preferred to an active method like thrusters, which require fuel. If the stabilization method was to use thrusters, the use of a drag sail would not be necessary, because a de-orbit maneuver could be done with the thruster. For rocket bodies it makes the most sense to utilize their existing geometry in the best possible way. For many of the rocket bodies that will be analyzed in this report, their length makes spin stabilization highly unlikely. Because of their mass moments of inertia, spin stabilization about an axis that would allow the drag sail to remain perpendicular to the drag vector is unstable in many of the vehicles.

For these reasons, gravity gradient was the obvious choice of stabilization for the rocket bodies equipped with their deployable drag sail. Figure 9 shows a cylindrical rocket body with a drag sail in a circular orbit. The rocket body in this figure is gravity gradient stabilized such that the drag sail is always perpendicular to the force of drag, causing the maximum cross sectional surface area to be exposed, and the maximum amount of drag to be utilized. In order for the rocket body to be stabilized using gravity gradient stabilization, the rocket body must be able to maintain its principal axes aligned with the orbital frame without the use of thrusters or any other active device. This definition imposes some restrictions on which geometries can actually be stabilized using this method. Because of these restrictions, a discussion about the mass moments of inertia of the rocket bodies is necessary to discuss stability.

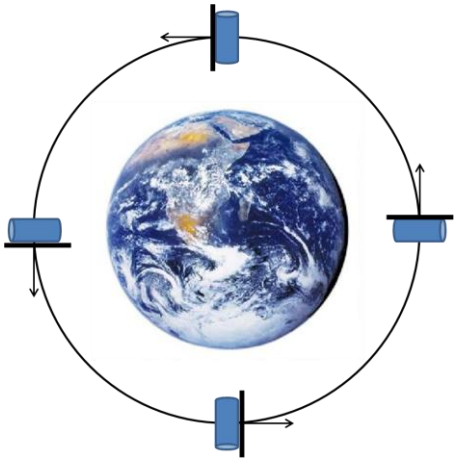

Figure 9. Gravity Gradient Stabilization

The mass moments of inertia for the rocket bodies in this report will be modeled as simple cylinders. The equations for the mass moments of inertia for a cylinder are shown below,

$$I_x = \frac{1}{4}mr^2 + \frac{1}{12}mL^2 \tag{41}$$

$$I_y = I_x \tag{42}$$

$$I_z = \frac{1}{2}mr^2 \tag{43}$$

where m is the mass of the rocket body, r is the radius of the rocket body, and L is the length of the rocket body.[15] The z-axis is along the length of the rocket body through the center of the circular ends, and the x and y axes complete the triad. At this point in order to simplify the mathematics three simplifying constants need to be introduced. These constants are shown in the equations below and are simply combinations of the mass moments of inertia.[14]

$$\sigma_x = \frac{(I_y - I_z)}{I_x} \tag{44}$$

$$\sigma_y = \frac{(I_x - I_z)}{I_y} \tag{45}$$

$$\sigma_z = \frac{(I_y - I_x)}{I_z}. \tag{46}$$

Now the angular equations of motion need to be defined in order to set up the stability conditions that will be necessary for gravity gradient stabilization. Those angular equations of motion are listed below.[14] Since there are no control torques or wheel induced angular momentum, those variables are equal to zero in these equations of motion. The resulting equations of angular motion are

$$T_{dx} = I_x\ddot{\phi} + 4{\omega_0}^2(I_y - I_z)\phi - \omega_0(I_x + I_z - I_y)\dot{\psi} \tag{47}$$

$$T_{dz} = I_z\ddot{\psi} + {\omega_0}^2(I_y - I_x)\psi + \omega_0(I_z + I_x - I_y)\dot{\phi} \tag{48}$$

$$T_{dy} = I_y\ddot{\theta} + 3{\omega_0}^2(I_x - I_z)\theta \tag{49}$$

where φ, ψ, and θ are the angles about the x, z, and y axes respectively in radians, and ω_0 is the orbital frequency in rad/s. The angular motion about the x and z axes are noticeably different than the angular motion about the y-axis. For this reason there will be two different stability analyses done for stability about those axes.[13] By taking the Laplace transformation of Eq. 50, a characteristic equation of the motion about the y-axis can be found to be

$$s^2 + \frac{3{\omega_0}^2(I_x - I_z)}{I_y} = 0 \tag{50}$$

and yields only one unstable root that occurs when I_x is greater than I_z. This is the only constraint for stability about the y-axis, but the stability conditions that are required to maintain stability about the x and z axes are much more stringent. Rearranging equations 47 and 48 and taking the Laplace transformation of those rearranged equation yields the following determinant

$$s^4 + {\omega_0}^2[3\sigma_x + \sigma_x\sigma_z + 1]s^2 + 4{\omega_0}^4\sigma_x\sigma_z = 0, \tag{51}$$

which when placed in term of s^2 allows for an equation that can be analyzed for stability conditions. This stability equation in terms of s^2 becomes

$$\frac{s^2}{{\omega_0}^2} = \frac{-(3\sigma_x+\sigma_x\sigma_z+1) \pm \sqrt{(3\sigma_x+\sigma_x\sigma_z+1)^2 - 16\sigma_x\sigma_z}}{2}. \tag{52}$$

Equation 52 yields three stability conditions after analyzing the roots of the equation. The term underneath the square root must be positive, and because of this the following three conditions for stability must be fulfilled.

$$3\sigma_x + \sigma_x\sigma_z + 1 > 4\sqrt{\sigma_x\sigma_z} \tag{53}$$

$$\sigma_x\sigma_z > 0 \tag{54}$$

$$3\sigma_x + \sigma_x\sigma_z + 1 > 0 \tag{55}$$

These three inequalities can be plotted onto a $\sigma_x - \sigma_z$ plane to show the classic stability region plot in Figure 10. This plot shows which combinations of moments of inertia will allow for stability about the x and z axis for gravity gradient stabilization. These conditions along with the stability condition that pertains to the y-axis describe the requirements for stability using this method.[14]

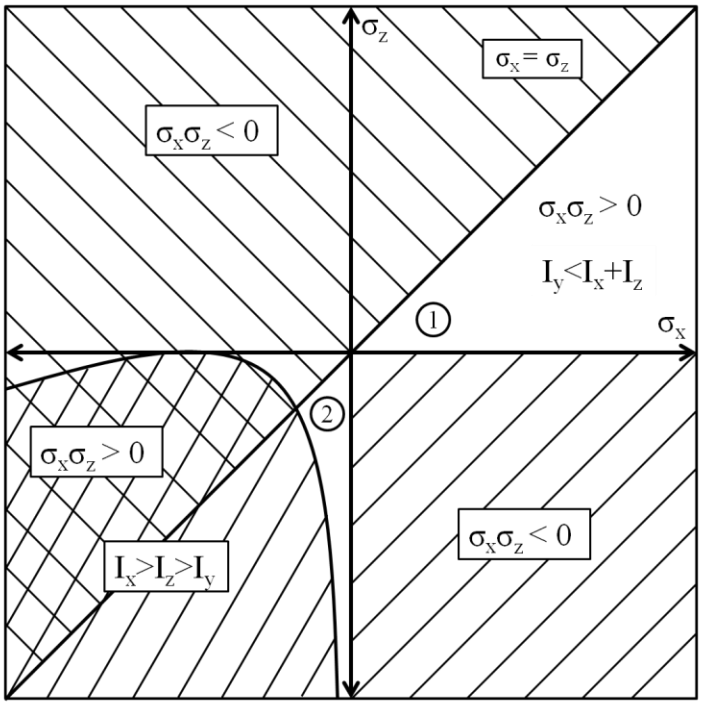

Figure 10. Gravity Gradient Stability Regions

In order for the body to be stabilized using gravity gradient stabilization, the spacecraft must either fall in section 1 or 2 of this stability region graph. Once it has been determined that the spacecraft will be stabilized using gravity gradient stabilization, the analysis of how the spacecraft reacts to the natural torques can begin. For this analysis, it has been assumed that disturbance torques about the x and z axes are negligible and they have not been taken into account. It has also been assumed that the body starts in an orientation that allows it to be gravity gradient stabilization. No maneuvers are done to put the body into an initial position after payload or stage separation.

The first thing that needs to be discussed is the specific natural torque being analyzed, and how it was calculated. The natural torque being considered for this gravity gradient stabilization analysis is the torque caused by the drag force. The drag force is not a force that is concentrated at a specific point, but it is rather a distributed load along the length of the sail. Figure 11 shows the distributed load that has been assumed for this analysis. The distributed load was concentrated into a single load and was applied to the sail at the location of the centroid of the distributed load. The distributed load shown in Figure 11 is exaggerated to show that there is a difference in drag between the top and bottom of the sail. The difference in drag between the top and bottom has been considered linear for ease of computation, and because the difference between the top and bottom force is so small that the type of distribution of the distributed load does not have a very noticeable effect. The other thing to notice in Figure 11 is the exaggerated effect that the drag force will have on the spacecrafts orientation. As the force of drag continually pushes on the lower half of the sail with a stronger force than the upper half, the body will begin to tilt in the direction shown by the cylinder drawn with dashed lines. The angle about the y-axis shown in Figure 6 is of particular interest as time goes on. As this angle changes, so does the cross sectional area exposed to the force of drag, and the goal is to have the maximum cross sectional area exposed to the drag vector at all times. The time response about the y-axis, or the pitch axis, is dependent partially on the geometry. If $I_x < I_z$ then one of the roots of the stability equation will be unstable and the pitch will change exponentially as time goes on. If the body has neutral stability, which means $I_x = I_z$, the time response of the pitch angle can be found using the equation below

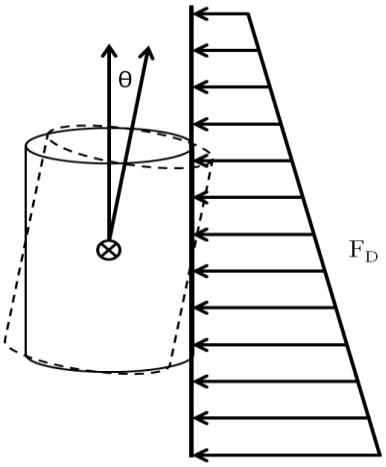

Figure 11. Drag Distributed Load

$$\theta(t) = \theta(0) + \dot{\theta}(0)t + \frac{T_{dy}t^2}{2I_y} \tag{56}$$

where t is the time that the body is exposed to the torque, T_{dy} is the torque about the y-axis, θ is the pitch, and the first two terms to the right of the equals sign are initial conditions for the pitch angle and change in pitch angle. A fully stabilized gravity gradient spacecraft has the mass moment of inertia relationship of $I_x > I_z$ and has a pitch angle time response that follows the relationship shown in the following equation

$$\theta(t) = \frac{T_{dy}}{I_y 3{\omega_0}^2 \sigma_y}\left[1 - \cos\left(\omega_0\sqrt{3\sigma_y}t\right)\right]. \tag{57}$$

This equation and its derivatives are the equations primarily used to include the pitch angle in the drag analysis.[14] The results of the pitch angle analysis as well as the stability of the rocket bodies will be discussed in the Stability and Angle of Attack section of this report.

IV. Results

The following sections will analyze the products of the analysis detailed in the previous sections. These results take into account all of the orbital perturbations and stability concerns listed in the analysis section. The first section will examine the effect that different drag sail sizes have on the time it takes to de-orbit a rocket body. This section will discuss a variety of sail sizes and ultimately select one size for further analysis. The second part of this results section takes the sail size that was chosen in the first section and performs the stability analysis for all of the rocket bodies being analyzed. For the first section not all of the rocket bodies that were analyzed have results shown. The results for the rocket bodies not shown can be found in Appendix F.

A. De-Orbiting Various Rocket Bodies With Various Sail Sizes

The first and most important question to analyze is whether or not a drag sail will actually make a difference or not during the de-orbiting process for a second or third stage rocket body. In order to do that, the drag sail size was varied for a number of different rocket bodies at a number of different altitudes. The rocket bodies that were analyzed in this report include the second stage of a Delta II, the second stage of a Delta IV, the second stage of an Atlas V, the second stages of both the Falcon 1 and Falcon 9, and the Pegasus XL. The results of this analysis for all of the vehicles can be seen in Appendix F, but for the body of this report, in order to demonstrate the usefulness of the drag sail on both the small and large rocket bodies, This report will focus primarily on the Pegasus XL to represent the smaller rocket bodies, and the Delta IV second stage to represent the larger rocket bodies.

For each rocket body, the sail size was varied from 0 m^2 to 50 m^2 in increments of 10 m^2. These 6 sizes for the drag sail (one size being no drag sail at all) were then placed on the rocket bodies at the same starting altitude which was also varied from 200 km to 500 km in increments of 100 km. The following four graphs correspond to these results for the Pegasus XL as it de-orbits using the various drag sail sizes.

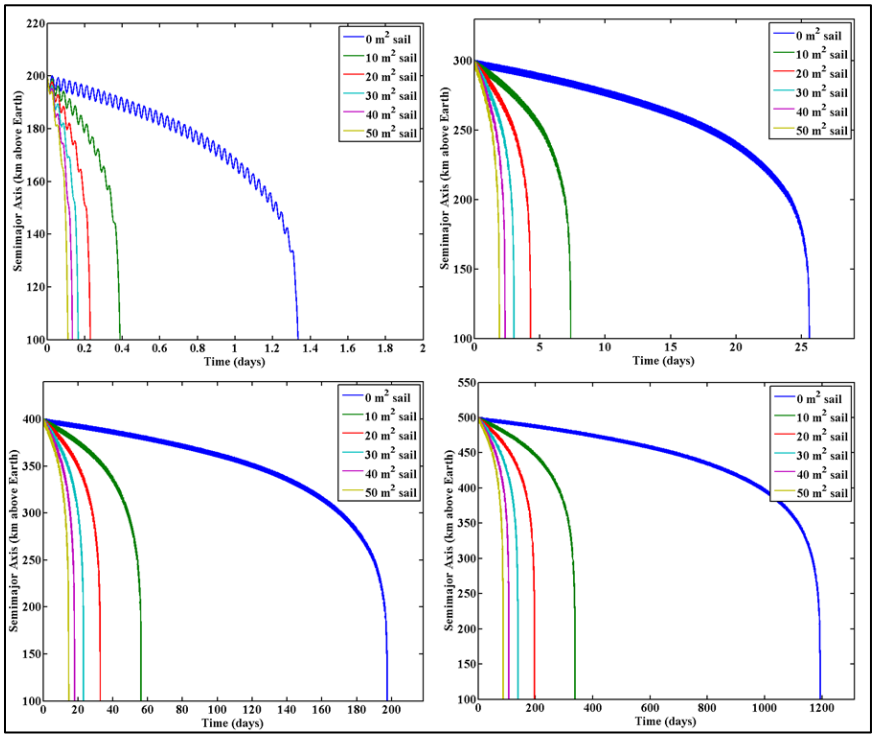

Figure 12. Orbital Decay of Pegasus XL for Various Sail Sizes

From these charts it is clear that the drag sail, in any size, will have a significant effect on the de-orbit time. At the lowest starting altitude, the drag sail decreases the orbit time by about 72% using the 10 m^2 sail, and at the highest starting altitude of 500 km, the drag sail decreases the orbit time by an 68%. This type of percentage is also consistent for the 300 and 400 km cases, as their de-orbit time is decreased by 71% and 70% respectively. The trend in these percentages shows that as the starting altitude of the orbit increases, the percentage of time that a drag sail can cut from a de-orbit lifetime decreases, but not by much. The percentage may be lower, but the amount of actual time that is saved is much greater. With the maximum drag sail size of 50 m^2 at the highest analyzed starting orbit of 500 km, the drag sail decreases the orbit lifetime by 91% and over 3 years. The minimum starting altitude with a 50 m^2 sail decreases the orbit lifetime by a higher percentage of 93%, but only decreases the de-orbit time by 1.3 days.

These results are quite different than the results of the Delta IV heavy. The Delta IV heavy results are shown in the figure below for the same range of starting altitudes and sail sizes

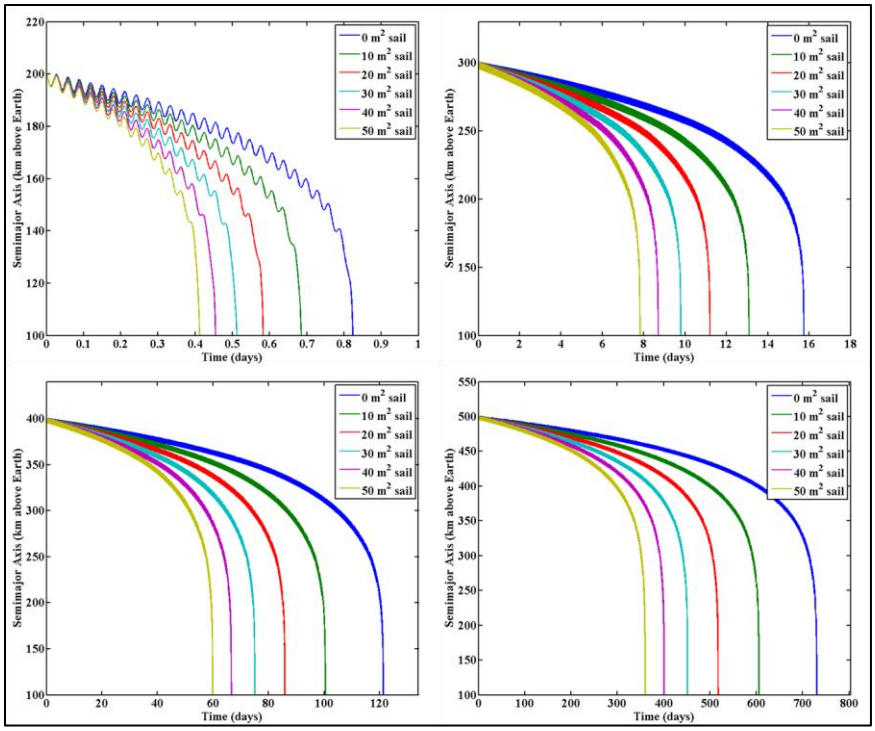

Figure 13. Orbital Decay of Second Stage Delta IV for Various Sail Sizes

The Delta IV sees a very different result than did the Pegasus XL. Because of its large mass, the Delta IV second stage does not respond nearly as strongly to the drag sail, but it still responds strongly enough. The 10 m^2 drag sail decreases the four orbits by an average of 16.25%, and the 10 m^2 drag sail decreases the orbit life from 720 days to about 605 days for a starting altitude of 500 km. The effects are not as severe as the effects seen by the Pegasus XL, but the effects are still noticeable and still reduce the orbital lifetime by a significant amount.

One of the questions that these graphs can answer is which sail size would be the optimum one to choose for a standard drag sail size. Immediately it would seem that the sail size that de-orbits the body the fastest would be the obvious choice. But for practicality and implementation reasons, it seems more reasonable to choose a sail size that significantly decreases the de-orbit time, but would not be unreasonably large. To make the selection for which sail size to analyze in the next section, the Pegasus XL graphs were used. In the Pegasus XL analysis it appears that there is a large difference between the de-orbit time between no sail and a 10 m^2 sail, and there is also a sizeable difference between the de-orbit time for a 10 m^2 sail and a 20 m^2 sail. The difference in de-orbit time for a 20 m^2 sail and a 30 m^2 sail is not as large, and the 40 and 50 m^2 sails have been deemed too large to practically consider. For these reasons the 20 m^2 sail has been chosen as the optimal sail size based on the results for all of the rocket bodies, but particularly on the smaller bodies, where there are larger jumps in de-orbit times for different area sizes.

B. Stability and Angle of Attack

The previous results clearly show that the rocket bodies examined in this study de-orbit quickly, and de-orbit even more quickly with the aid of the drag sail. But one of the most important questions is whether the rocket is stable as it orbits, and how well does the body keep the drag sail in the drag vector.

The question as to whether the rocket body will remain stable using gravity gradient stabilization can be answered by using the mass moments of inertia of the rockets, the simplifying factors in Eqs. 44-46, and examining the stability plot from Figure 10. Using the mass moment of inertias and the simplification factors, the stability locations of each of the utilized rocket bodies is shown in the figure below. The quantity σ_x from Eq. 44 is along the horizontal axis of this plot, while the quantity σ_z from Eq. 46 is along the vertical axis.

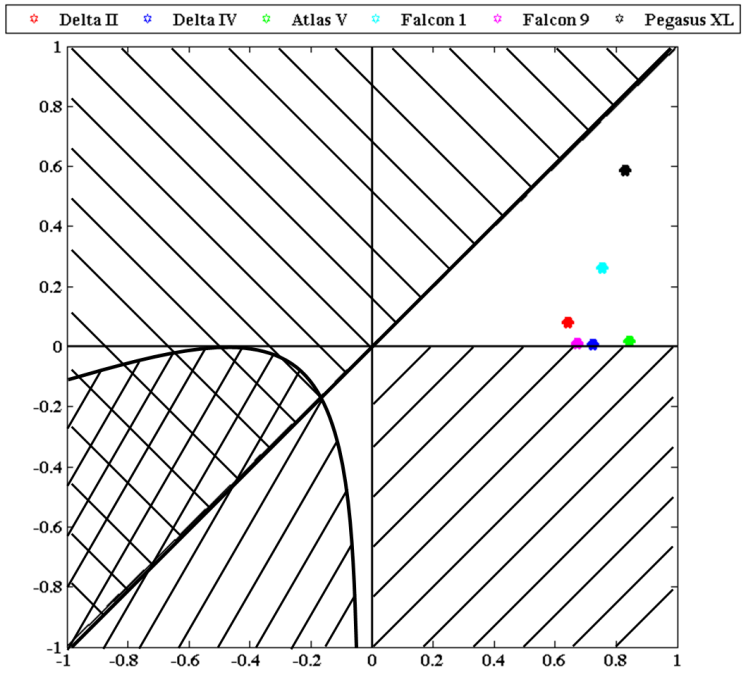

Figure 14. Gravity Gradient Stability Plot for Rocket Bodies

Although it appears that the Atlas V, Delta IV, and Falcon 9 look to be dangerously close to a region of instability, their pitch axes remain stable and do not diverge in an unacceptable fashion. One thing to notice from this plot is that the three longer rocket bodies are the three that sit close to the region of instability, while the three rocket bodies that have smaller length to diameter ratios sit more towards the center of the stable region. It should be noted however, that rocket bodies with too small of a length to diameter ratio will become inherently unstable as oblate spinners and will not function well with this drag sail. Despite the close proximity of the Falcon 9, Delta IV heavy, and Atlas V rocket bodies to the region of instability, their pitch axes vary quite similarly to the other three rocket bodies. That is, they are no less stable than the other three despite their location on the chart. This fact is shown below in Figure 15, which shows all of these rocket bodies and their pitch angle over time as the bodies de-orbit from 400 km.

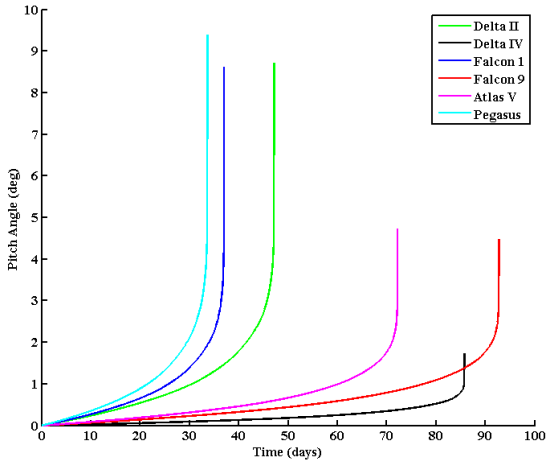

Figure 15. Pitch Angle Over Time for 400 km Decay

The pitch angle, also known as angle of attack in this case, appears a slow and smooth increase followed by a sharp and large increase at the end. The reason for the large upturn at the end of each of the graphs, is that when the force of drag is getting larger and larger, it starts to affect the pitch angle more and more. At the end of their

orbital decay none of these pitch angles are in excess of 10 degrees, and at this point in the mission lifetime, they are sure to de-orbit after just a few hours regardless of how much surface area is in the drag vector. The three larger vehicles seem to experience less of a change in pitch angle than do the three smaller vehicles, and this is because the larger masses of those vehicles make it difficult to alter their orientations, whereas the less massive vehicles can be more easily influenced.

V. Conclusion

Utilizing the force due to atmospheric drag when de-orbiting spacecraft is a common practice and one of the most effective ways to reduce the de-orbit time of a space vehicle. Drag enhancing mechanisms have historically been designed for small satellites, and have tested with very favorable results, which lead to the conclusion that a drag enhancing mechanism would also perform well on larger space vehicles. By using a drag enhancing mechanism such as a drag sail, along with several other orbital perturbations, should help reduce the time it takes larger vehicles such as rocket bodies to de-orbit. The objective of this report is to produce adequate computational evidence that such a drag sail, when used on a variety of rocket bodies, will de-orbit a rocket body in significantly less time than if no drag sail were used.

The analysis performed in this report provides sufficient computational evidence that the use of a drag sail, in any size, will have a positive effect on the time it takes to de-orbit a rocket body. This report has implemented such a drag sail onto six different launch vehicle stages including a Delta IV, Delta II, Falcon 1, Falcon 9, Atlas V, and a Pegasus XL, all of which have shown a decrease in de-orbit time when equipped with a drag sail. It has shown a 20 m^2 sail is a preferable balance between optimized de-orbit time and practical implementation, and it has also been shown that the rockets will remain stable throughout their de-orbit using gravity gradient stabilization. The chosen sail size decreases the de-orbit time for the Pegasus XL by an average of 84% for altitudes of 200 km, 300km, 400km, and 500 km, and decreases the de-orbit time for a Delta IV second stage by an average of 16.25% for the same range of altitudes.

This report serves as an adequately accurate representation of what a gravity gradient stabilized rocket body will experience while using a drag sail to decrease the de-orbit time. Some of the perturbations used in this report could use models with increased accuracy such as the J_2 perturbations and the density model used for the atmospheric drag model, but the models used in this report are commonly used for detailed analysis. In order to progress in the design of the sail discussed in this report there are many other things that need to be considered. The packing and deployment of the sail, as well as the material that the sail is made of need to be explored, and a deeper look into beginning of life attitude and control needs to be done.

Appendix A – Earth's Zonal Coefficients

The following coefficients are from Coffey, Deprit, and Deprit.

Zone	Zonal Coefficient
J_2	1.082635e-3
J_3	-2.54321530e-6
J_4	-1.6109877e-6
J_5	-2.3578565e-7
J_6	5.431685e-7

Appendix B - Greenwich Sidereal Time Algorithm

The algorithm for calculating the Greenwich sidereal time requires the knowledge of the Julian date number, J_0, and the universal time, UT in hours. The following algorithm is from Vallado and calculates the Greenwich sidereal time in degrees.

$$T_0 = \frac{J_0 - 2451545}{36525}$$

$$\theta_0 = 100.4606184 + 36000.77004T_0 + 0.000387933{T_0}^2 - (2.583 \times 10^{-8}){T_0}^3$$

$$\theta = \theta_0 + 360.98564724\frac{UT}{24}$$

A diagram is shown as a visual representation of this algorithm.

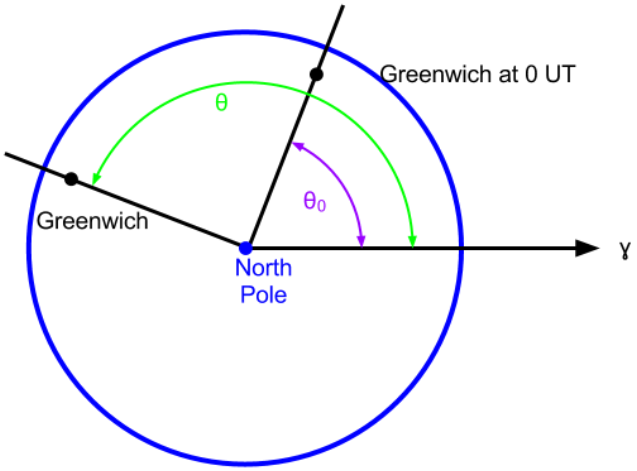

Appendix C – Block Diagram of J_2 through J_6 Calculation

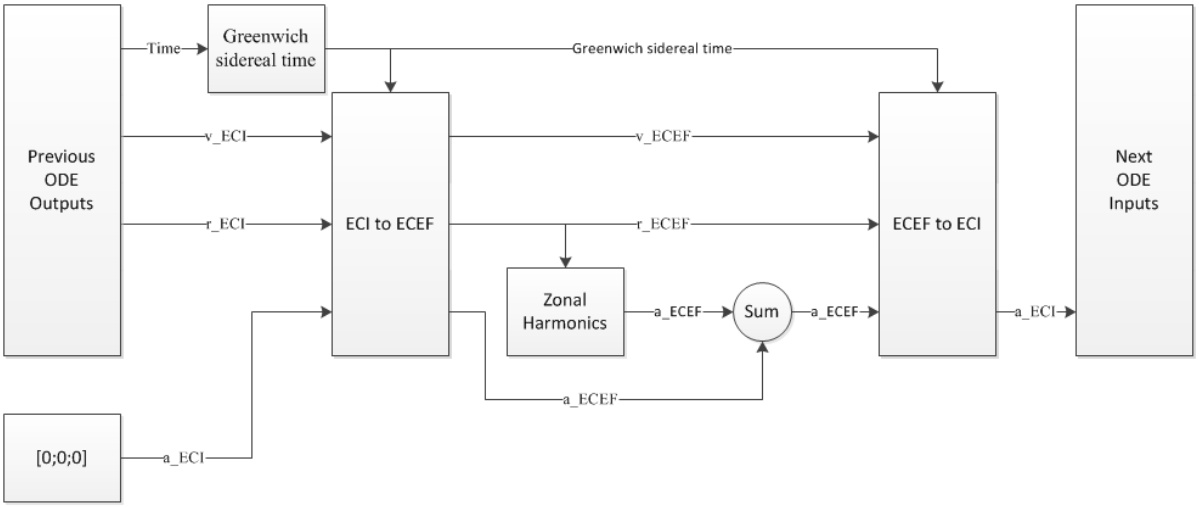

Appendix D – Earth to Sun Position Vector Algorithm

To calculate the position vector of the Sun in the ECI frame the only needed input is the Julian date, *JD*. The following algorithm is from Vallado;

$$T = \frac{JD - 2452545.0}{36525}$$

$$\lambda_{M_\odot} = 280.460° + 36000.771T$$

$$M_\odot = 357.5277233° + 35999.05034T$$

$$\lambda_{ecliptic} = \lambda_{M_\odot} + 1.914666471° \sin(M_\odot) + 0.019994643 \sin(2M_\odot)$$

$$r_\odot = 1.000140612 - 0.016708617 \cos(M_\odot) - 0.000139589 \cos(2M_\odot)$$

$$\epsilon = 23.439291° - 0.0130042T$$

$$\vec{r}_{\oplus\odot} = r_\odot \begin{bmatrix} \cos(\lambda_{ecliptic}) \\ \cos(\epsilon)\sin(\lambda_{ecliptic}) \\ \sin(\epsilon)\sin(\lambda_{ecliptic}) \end{bmatrix} \text{AU}$$

where 1 AU is the average distance from the Sun to the Earth, approximately 1.49597871e8 km.

Appendix E – Earth to Moon Position Vector Algorithm

To calculate the position vector of the Moon in the ECI frame the only needed input is the Julian date, *JD*. The following algorithm is from Vallado;

$$T = \frac{JD - 2452545.0}{36525}$$

$$\begin{aligned} \lambda_{ecliptic} = {} & 218.32° + 481267.883T + 6.29 \sin(134.9 + 477198.85T) - 1.27 \sin(259.2 - 413335.38T) \\ & + 0.66 \sin(235.7 + 890534.23T) + 0.21 \sin(269.9 + 954397.7T) \\ & - 0.19 \sin(357.5 + 35999.05T) - 0.11 \sin(186.6 + 966404.05T) \end{aligned}$$

$$\begin{aligned} \phi_{ecliptic} = {} & 5.13° \sin(93.3 + 483202.03T) + 0.28 \sin(228.2 + 960400.87T) - 0.28 \sin(318.3 + 6003.18T) \\ & - 0.17 \sin(217.6 - 407332.2T) \end{aligned}$$

$$\begin{aligned} \wp = {} & 0.9508° + 0.0518 \cos(134.9 + 477198.85T) + 0.0095 \cos(259.2 - 413335.38T) \\ & + 0.0078 \cos(235.7 + 890534.23T) + 0.0028 \cos(269.9 + 954397.7T) \end{aligned}$$

$$\bar{\epsilon} = 23.439291° - 0.0130042T - 1.64 \times 10^{-7} T^2 + 5.04 \times 10^{-7} T^3$$

$$r_\leftmoon = \frac{1}{\sin \wp}$$

$$\vec{r}_\leftmoon = r_\leftmoon \begin{bmatrix} \cos(\phi_{ecliptic})\cos(\lambda_{ecliptic}) \\ \cos(\bar{\epsilon})\cos(\phi_{ecliptic})\sin(\lambda_{ecliptic}) - \sin(\bar{\epsilon})\sin(\phi_{ecliptic}) \\ \sin(\bar{\epsilon})\cos(\phi_{ecliptic})\sin(\lambda_{ecliptic}) + \cos(\bar{\epsilon})\sin(\phi_{ecliptic}) \end{bmatrix} RE$$

where *RE* is the average radius of the Earth, 6378 km.

Appendix F – Varying Sail Size for Various Rocket Bodies

Delta II

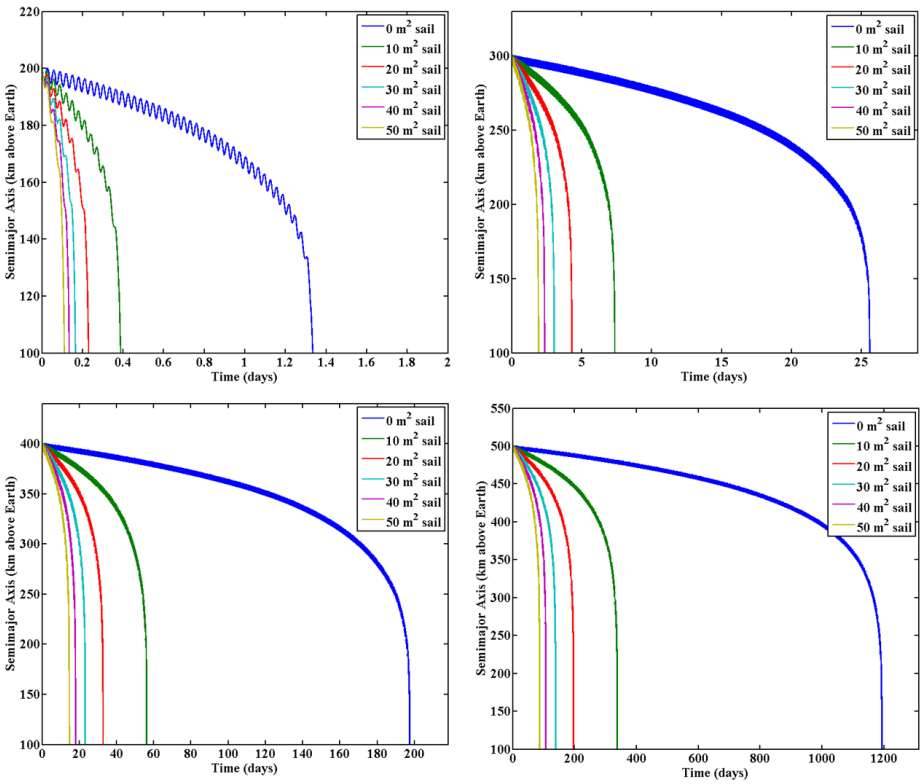

Atlas V

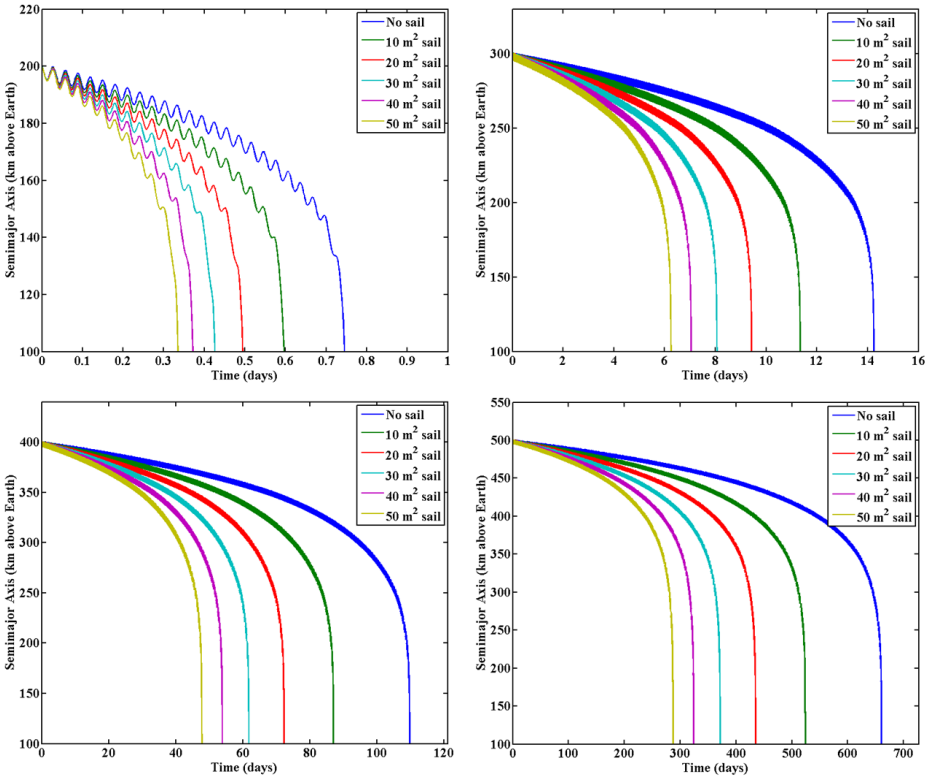

Falcon 1

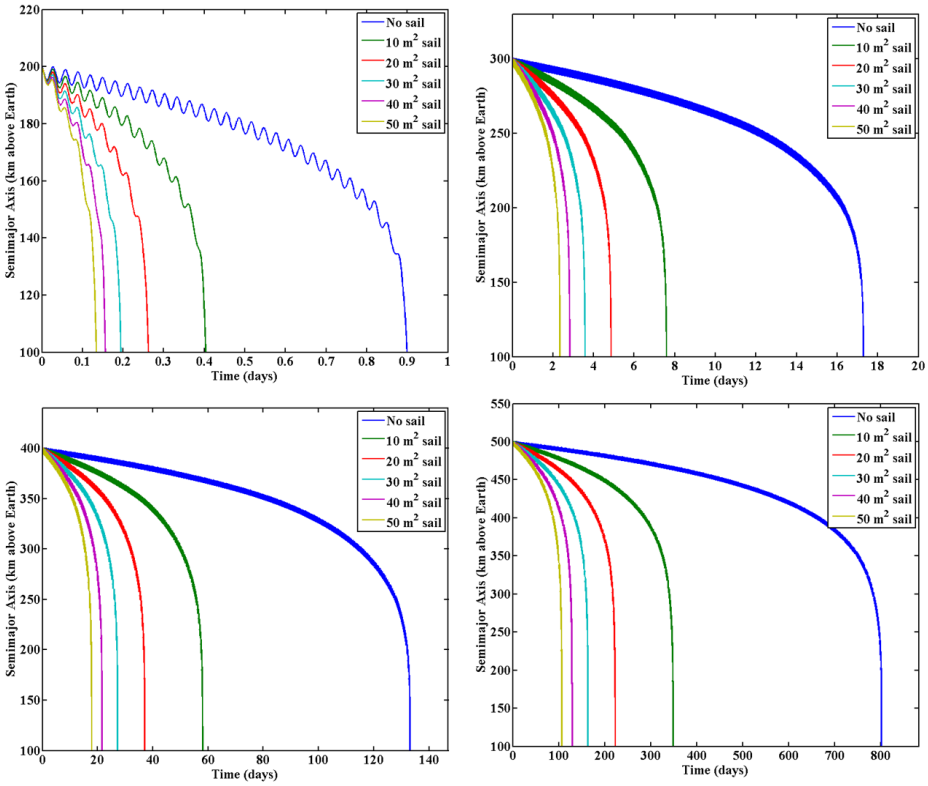

Falcon 9

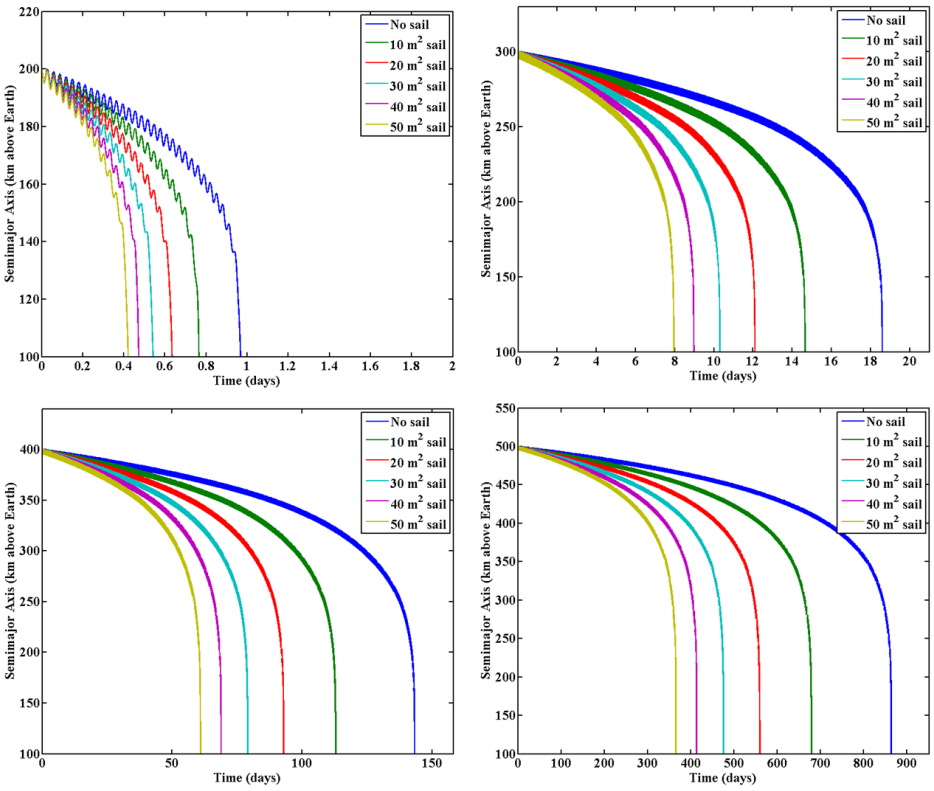

Appendix G – MATLAB Code

If you would like to obtain a copy of the MATLAB codes used, please contact the Aerospace Engineering Department at kabercro@calpoly.edu.

Acknowledgments

The authors would like to acknowledge Dr. Kira Abercromby, the advisor for this project, for all of her guidance.

References

[1] Larson, W. J., and Wertz, J. R., *Space Mission Analysis and Design*, 3rd ed., Micrososm Press, 2010, pp. 139-140.

[2] "Monthly Number of Objects in Earth Orbit by Object Type," *Orbital Debris Quarterly News*, Vol. 16, No. 1

[3] Stansbery, E., "Orbital Debris Frequently Asked Questions," *NASA Orbital Debris Program Office* [online webpage], URL: http://orbitaldebris.jsc.nasa.gov/faqs.html [cited: 8 June 2012].

[4] "NASA Procedural Requirements for Limiting Orbital Debris," NASA Office of Safety and Mission Assurance.

[5] "Process for Limiting Orbital Debris," NASA-STD-8719.14A, 8 December 2012.

[6] Anselmo, L., Cordelli, A., Jehn, R., Pardinim C., Rossi,. A., Effect of Mitigation Measures on the Long-Term Evolution of the Debris Population, *Adv. Space Res.* Vol. 28, No. 9, pp. 1427-1436,200l

[7] Ash, R. L., and Lokcu, E., "A De-orbit System Design for CubeSat Payloads."

[8] Maessen, D. C., "Development of a generic inflatable de-orbit device for CubeSats," M.S. Thesis, Aerospace Engineering Dept., Delft University of Technology, Delft, Netherlands, 30 May 2007.

[9] Lucking, C., Colombo, C. and, Mcinnes, C., "A passive high altitude deorbiting strategy," *25th Annual IAA/USU Conference on Small Satellites*, Logan, Utah, 8 August 2011.

[10] Pisacane, V. L., *The Space Environment and Its Effects on Space Systems*, AIAA, 2008.

[11] Curtis, H. J. *Orbital Mechanics for Engineering Students*, 2nd ed., Elsevier, 2010, pp. 278.

[12] Vallado, D. A. *Fundamentals of Astrodynamics and Applications*, 3rd ed., Microcosm Press, 2007.

[13] Escobal, P. R., *Methods of Orbit Determination*, John Wiley & Sons, Inc., New York, 1965, pp. 49.

[14] "Astrodynamic Coordinates," *Orbital Mechanics with Numerit* [online document], URL: http://www.cdeagle.com/omnum/pdf/csystems.pdf [cited: 8 June 2012].

[15] Sidi, M. J., *Spacecraft Dynamics & Control: A Practical Engineering Approach*, Cambridge University Press, 1997.